Reversible Mechanical and Electrical Properties of Ripped Graphene

J. Henry Hinnefeld,[1] Stephen T. Gill,[1] Shuze Zhu,[2] William J. Swanson,[1] Teng Li,[2] and Nadya Mason[1,*]
[1]*Department of Physics, University of Illinois at Urbana-Champaign, 1110 West Green Street, Urbana, Illinois 61801, USA*
[2]*Department of Mechanical Engineering, University of Maryland, College Park, Maryland 20742, USA*

(Received 2 October 2014; revised manuscript received 20 October 2014; published 30 January 2015)

We examine the mechanical properties of graphene devices stretched on flexible elastomer substrates. Using atomic force microscopy, electrical transport measurements, and mechanics simulations, we show that microrips form in the graphene during the initial application of tensile strain; however, subsequent applications of the same tensile strain elastically open and close the existing rips. Correspondingly, while the initial tensile strain degrades the devices' transport properties, subsequent strain-relaxation cycles affect transport only moderately, and in a largely reversible fashion. Graphene's electrical and mechanical robustness even after partial mechanical failure is unique among conducting thin films. This understanding of the creation and dynamics of rips in graphene is relevant to the design of flexible graphene-based devices which are required to function under strain.

DOI: 10.1103/PhysRevApplied.3.014010

I. INTRODUCTION

Recent advances in graphene production [1–3] have enabled the fabrication of a variety of flexible, graphene-based electronic components, including transparent interconnects [4], high-performance capacitors [5], and transistors [6]. The prospect of flexible and transparent graphene-based electronic devices suggested by these results raises an important question: are graphene's electrical properties and mechanical integrity robust under the strains graphene is likely to experience in such devices? For example, some applications, such as frequency-tuned *RC* circuits using graphene capacitors and interconnects, would require careful consideration of what strains the device could withstand while keeping strain-induced variations in the electronic properties of graphene within the required specifications. Pristine graphene has an exceptionally high breaking strength [7], yet it may be susceptible to ripping, particularly if it has defects [8] and/or strong surface adhesion [9]. It is still relatively unknown under what strain conditions substrate-supported graphene rips, and how the electrical properties are then altered.

In this paper, we combine atomic force microscopy (AFM), coarse-grained mechanical simulations, and electrical transport measurements to study the effects of lateral strain on rips in graphene. We find that graphene adhered to a flexible substrate and then stretched laterally can develop small rips with only 1% applied strain. However, even with ripping, the electrical properties remain relatively robust: introducing small rips slightly increases the resistance, but subsequent strain-relaxation cycles over the same strain range change transport only modestly, and in a largely reversible fashion. The onset and dynamics of the rips with applied strain are consistent with simulations, which demonstrate that both the length and width of the rips saturate with constant strain, and that the original shape of the graphene is recovered when the strain is released. Such resilience is atypical for conducting thin films, which typically demonstrate rapid and irreversible device failure after the onset of rip formation [10,11]. This understanding of when and how graphene rips, and how its electrical properties are thereby altered, is directly applicable to the implementation and production of flexible graphene devices.

II. EXPERIMENTAL DETAILS

Devices consist of patterned graphene placed on flexible polydimethylsiloxane (PDMS) substrates. The devices are fabricated using a modified transfer printing process, similar to that described in Ref. [1]. Single-layer graphene is grown using established chemical vapor deposition (CVD) techniques [12], and then transferred to a copper-coated silicon wafer where it is patterned using photolithography and reactive ion etching. Next, a piece of PDMS is mechanically pressed onto the silicon wafer, and the copper is then etched to leave patterned graphene on the PDMS substrate [3]. Raman spectroscopy is used to confirm the presence of graphene on the PDMS as shown in Fig. 1(c); the shape of the Raman 2D peak [13], as well as subsequent AFM measurements, verify the single-layer character of the graphene. Finally, shadow-mask evaporation is used to deposit Ti/Au contact pads. The device geometry is illustrated in Fig. 1(a): a narrow graphene bridge connects two large graphene pads, each of which is covered with a Ti/Au contact pad. We study 13 different devices having bridge aspect ratios ranging from 1.5:1 to

---

[*] nadya@illinois.edu

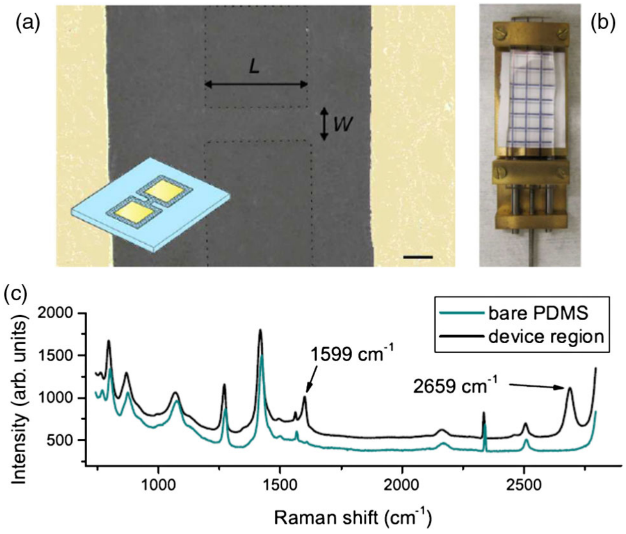

FIG. 1. (a) False-color optical image of a graphene bridge device (outlined by dashed line) patterned on a polydimethylsiloxane (PDMS) substrate with gold contact pads (light yellow). The length L and width W of the bridge are described in the text. The scale bar is 25 μm. Inset: A schematic illustration of the device geometry. (b) The mechanical stretching stage with PDMS inserted between the clamps. The devices are stretched along the axis of the microbridge. (c) Offset Raman spectra for a bare PDMS region and a graphene device region. The G and 2D peaks, at 1599 cm^{-1} and 2659 cm^{-1} respectively, in the spectra from the device region confirm the presence of graphene.

12:1 (length:width) and widths of 100, 50, and 25 μm. The data in this paper focus on a device with a bridge width of 25 μm and an aspect ratio of 2:1. The data for all samples yield similar qualitative results. Quantitative differences in transport data between different devices are uncorrelated with the bridge dimensions, and instead seem to be dominated by preexisting rips in the graphene, which are often introduced during the graphene transfer process [8].

AFM and transport measurements are performed while the PDMS substrate is mounted in a mechanical stretching stage, as shown in Fig. 1(b). The substrate is clamped at either end, and then strained by turning the threaded rod, which laterally moves the sliding clamp along its guide rails. A mechanical stepper motor is used to control the stretching stage position to ensure reproducibility. Variable device positioning on the substrate as well as slight variations in substrate thickness preclude exact conversion between strain applied to the substrate and to the device, therefore “turns of the stretching stage control rod” are used as the controlled variable. Each turn strains the substrate by approximately 1%. AFM topology and phase measurements show that most regions of the graphene (e.g., surrounding the rips) are firmly attached to the PDMS [14]; thus, the strain applied to the graphene should be proportional to the strain applied to the PDMS. We measure that the strain applied to the center of the sample where the graphene device is located differs by no more than 10% from the strain applied at the PDMS substrate edges. However, our conclusions are unaffected by this difference, as variations in the magnitude of applied strain between devices only shift the strain axis of the data while preserving the observed trends. Optical observations indicate that the Ti/Au pad adhesion to the substrate is robust and does not slip during measurements. AFM measurements are performed with an Asylum Research MFP-3D.

Transport measurements are performed by placing micromanipulator probes in contact with the gold contact pads in a two-point configuration. One hundred readings are taken at each strain value and the lowest reading is chosen for the plot (this value is taken as having the minimum contact resistance; the average value of the 100 readings gives similar values and trends as the minimum reading). The average spread in the readings at a given strain value is an order of magnitude smaller than the resistance variations observed due to changing strain.

III. RESULTS AND DISCUSSION

A. Topology of rips

Figures 2(a)–2(f) show AFM phase images of graphene in the bridge region of a device at 0%, 5%, 0%, 5%, 10%, and 0% strain applied along the horizontal axis of the images. Both rips and delaminations caused by wrinkles appear as a function of strain, and can be distinguished via AFM height data: Figs. 2(g) and 2(h) show that wrinkles have corresponding undulations in the height data (peaks and dips) while rips are indicated by a uniform depression (consistent with the substrate exposed between graphene regions). In Fig. 2, the vertical features are rips and the majority of the horizontal features are wrinkles. Measurements of bare substrate topology under identical conditions show essentially no surface variation, indicating that the observed features are intrinsic to the graphene, and are not a consequence of defect formation in the substrate.

The opening and closing of rips is clear in the figure: the unstrained device [Fig. 2(a)] exhibits some small rips and defects. When the substrate is mechanically stretched [Fig. 2(b)], the existing rips widen and new rips form; when the applied strain is relaxed [Fig. 2(c)], preexisting defects return to nearly their original condition and the edges of newly formed rips return to their original positions (but do not recover their original crystal structure). Subsequent strain-relaxation cycles over the same strain range reopen existing rips [Fig. 2(d)], but proceeding to a higher strain range forms new rips and widens preexisting ones [Fig. 2(e)], which then close less completely when the strain is relaxed [Fig. 2(f)]. The strain values at which we observe microrip formation are substantially lower than the reported fracture strength of graphene [7]; however, the tensile strength of graphene is strongly susceptible to defects such as holes and tears [15]. Although graphene

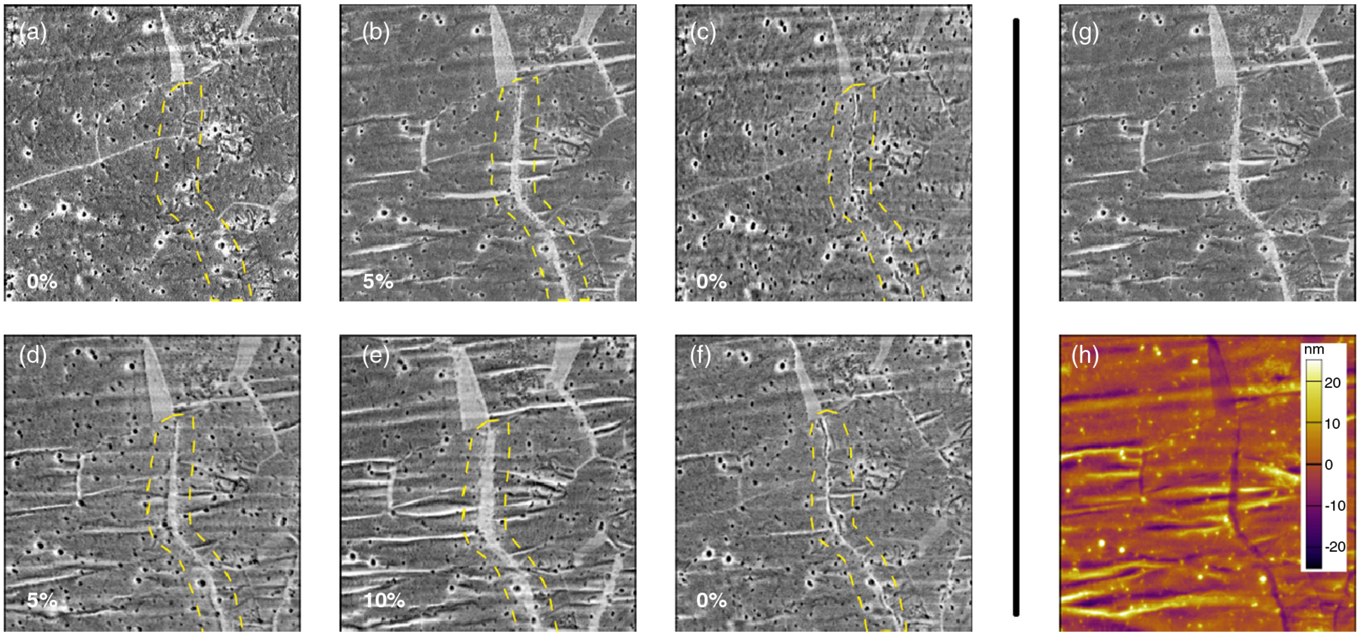

FIG. 2. (a)–(f) AFM phase measurements of graphene on a polymer substrate at approximately 0%, 5%, 0%, 5%, 10%, and 0% strain (applied along the horizontal axis), as labeled. Rips are evident as light gray, elongated vertical features. An example of a rip that opens and closes with applied strain is indicated by the dashed line. Dark spots present in each image are debris on the substrate surface; white halos surrounding some of the debris are indicative of graphene slightly delaminating from the substrate. Elongated horizontal features are strain-dependent wrinkles. (g) AFM phase and (h) height data. Variations in the height data distinguish between wrinkles and rips in the graphene, which have similar signatures in the phase data. The scanned area in each image is 25 $\mu\mathrm{m}^2$.

produced by CVD is known to be polydomain, it has been shown that rips in graphene do not preferentially follow grain boundaries [8]. Rather, the fabrication procedures used to generate patterned graphene devices on polymer substrates routinely introduce rips and other defects in the graphene, which accounts for the mechanical failure observed at low strain values.

B. Simulation of rip formation

To shed light on the underlying mechanism of the rip formation and evolution, we simulate rip formation and the subsequent elastic opening and closing of rips in graphene, via a coarse-grained (CG) modeling scheme [16]. Given the prohibitive simulation expense to model rips of real size in experiments (microns in length), we simulate a scaled-down model of a graphene monolayer with a size of 24 nm by 200 nm (Fig. 3). Three precracks of various sizes are introduced in the model [Fig. 3(a)] to mimic the preexisting defects in the as-made sample. Each CG bead in the graphene interacts with a virtual substrate via a Lennard-Jones potential [14] $V_{\mathrm{g.s.}}(r) = 4\varepsilon_{\mathrm{g.s.}}[(\sigma_{\mathrm{g.s.}}^{12}/r^{12}) - (\sigma_{\mathrm{g.s.}}^{6}/r^{6})]$, where $\varepsilon_{\mathrm{g.s.}} = 0.01844$ eV, and $\sigma_{\mathrm{g.s.}} = 0.29$ nm, which gives rise to an adhesion energy around 0.044 $\mathrm{eV/nm}^2$. In addition, the CG beads on the four outer edges of the simulation model are not allowed to slide relative to the substrate so that the tensile loading of the graphene can be applied by stretching the

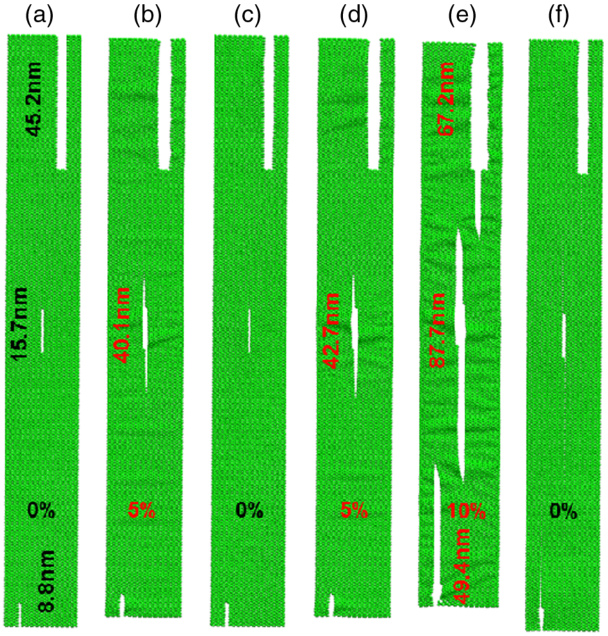

FIG. 3. Coarse-grained simulations show the elastic opening and closing of rips during initial and subsequent tensile loading cycles, in good agreement with AFM measurements in Fig. 2. The graphene region was simulated at 0%, 5%, 0%, 5%, 10%, and 0% strain applied along the horizontal axis, as labeled. Values given in nanometers refer to the rip lengths. The vertical contraction of the graphene region at higher strain values is due to the Poisson effect.

substrate along the horizontal direction, similar to the experimental setup.

As the applied tensile strain first increases to 5%, the stress concentration near the tips of the short middle crack (~15.7 nm in length) becomes sufficiently high to cause the propagation of the short crack in both directions. Due to the nature of displacement loading, the driving force for crack propagation decreases as the crack extends. As a result, the middle crack stops advancing at a length of ~40.1 nm [Fig. 3(b)]. Upon unloading of the tensile strain the elongated middle crack closes, nearly fully recovering the original shape of the graphene [Fig. 3(c)]; however, the atomic bond breaking in graphene during crack propagation is not reversible. Consequently, the graphene cannot fully recover its original mechanical integrity.

Further tensile loading up to 5% causes the cracks to reopen but further extension of the cracks is shown to be negligible [Fig. 3(d)], largely due to a lack of sufficient driving force for crack propagation. The application of a tensile loading of 10% provides sufficient driving force to cause all three cracks to extend significantly. The crack propagation eventually saturates due to the decreasing driving force under displacement loading [Fig. 3(e)]. Upon unloading to zero strain, all newly formed cracks close, resulting in a graphene morphology nearly identical to its original shape [Fig. 3(f)], similar to the experimental observation [Fig. 2(e) to Fig. 2(f)].

Simulations also show the formation of delaminations and horizontal wrinkles in graphene upon tensile loading and the disappearance of such features upon unloading, which agrees with the experimental observations (Fig. 2). We attribute the formation of these delamination and wrinkle features to the combined effect of a mismatch in Poisson's ratios between graphene and the PDMS substrate and the relatively weak graphene-PDMS interfacial bonding. In addition, recent studies show that the location of wrinkles in graphene can be guided by the debris distribution on the substrate surface [17], consistent with our experimental observations in Fig. 2.

Our simulations of the onset and dynamics of the rips with applied strain are consistent with experimental observations; we take the close fit between simulations and experiment as evidence for the likely validity of the simulations. Both simulations and experiments show that rips form in the graphene at strains well below its intrinsic breaking strength; experimentally, we observe rip formation at strains as low as 1% applied strain. Concerning the dynamics of the rips, we again find excellent agreement between experiment and simulation, with both showing that the rips saturate, rather than continue along a line as often happens in other materials [10,11]. Finally, both show that, remarkably, the rips close with unloading of tensile strain, nearly fully recovering the original shape of the graphene.

C. Electrical transport measurements

The behavior of the rips determines the electrical transport as a function of strain, as evident in Fig. 4. Figure 4(a) demonstrates three important features of the data: first, during the initial application of strain (*A* to *B* in the figure), the resistance increases (for this sample, by approximately 43%). Typical values for this initial increase in other devices ranged from 20% to 40% of the starting resistance. Second, the resistance of the device decreases as the applied strain is relaxed (from *B* to *C*) by 7% for this device, and typically by between 6% and 14%. Finally, in subsequent strain-relaxation cycles over the same strain range, the resistance changes only moderately, and in a largely reversible fashion.

The transport behavior can be explained by the opening and closing of rips: in the unstrained device, small rips largely determine the initial resistivity. The device's resistance increases when the substrate is mechanically stretched, due to the widening of existing rips and formation of new

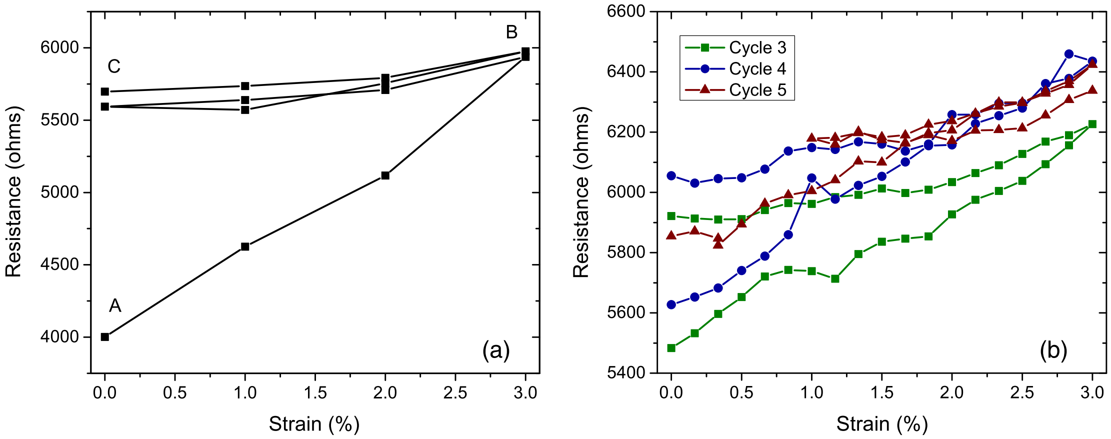

FIG. 4. (a) Electrical resistance of a graphene device vs applied tensile strain. The initial application of strain significantly increases the resistance while subsequent strain-relaxation cycles over the same strain range yield smaller, mostly reversible changes in the resistance. (b) Three consecutive strain-relaxation cycles (cycles 3, 4, 5), showing largely reversible transport characteristics.

ones; subsequent strain-relaxation cycles over the same strain range, which reopen and close existing rips, generate largely reversible changes in resistance. This reversibility is demonstrated in Fig. 4(b); data from the same device recorded during the third, fourth, and fifth strain-relaxation cycles are shown in green, blue, and red, respectively. In each case, the resistance changes by ~14% for ~3% applied strain, and returns to within 8% of its original value. Proceeding to a higher strain range forms new rips, consistent with a jump in resistance when the strain range is increased. This behavior—an increase in resistance with the initial application of tensile strain, followed by moderate and reversible changes in the resistance during subsequent strain-relaxation cycles over the same strain region—persists up to approximately 15% applied strain, at which point the devices become permanently nonconducting.

Previous experimental work has demonstrated reversible transport changes in strained graphene, either by depositing graphene on prestrained substrates so as to create controlled crumpling [18] and buckling [19], by patterning complex interconnect geometries [3,4], or by measuring transport across macroscopic graphene films [1,2]. In comparison, this work demonstrates the continuing robustness of device functionality *after* partial mechanical failure. Such resilience is distinctly atypical for conducting thin films: similar studies performed on tin-doped indium oxide (ITO) [10] and zinc oxide [11] reported rapid and irreversible device failure after the onset of rip formation. One potential explanation for graphene's exceptional resilience is its morphological simplicity: as a two-dimensional membrane, reestablishing electrical contact between two sides of a rip is as simple as overlaying two sheets of paper, while for typical three-dimensional thin films, the process is more similar to fitting two halves of a snapped pencil back together.

IV. CONCLUSION

In summary, we have observed the formation and subsequent evolution of microrips in graphene using atomic force microscopy. Mechanics simulations further reveal the underlying deformation and failure mechanisms of the graphene sample under initial and subsequent cyclic tensile loadings, which agree well with the AFM measurements. Defects such as rips commonly appear in graphene transferred to surfaces, and these rips then dominate the graphene's mechanical and electronic properties as a function of strain. We demonstrate the scale of typical rip evolution: the length and width increase by a factor of 2–3 for 5% applied tensile strain. We also demonstrate that, while an initial application of tensile strain introduces new mechanical defects, successive strain-relaxation cycles over the same strain range elastically open and close the existing rips. This mechanical effect has a corresponding electrical effect: the graphene's transport properties are degraded by the initial application of strain, but show small, mostly reversible changes during ensuing strain-relaxation cycles. Graphene's combination of superlative electronic properties, extreme flexibility, and robust functionality after partial mechanical failure is unique among conducting thin films and lends itself to a variety of promising future device applications. While the design of such devices may be limited by the low strain values at which graphene rips, this may be balanced by the saturation and healing of the rips after they form.

ACKNOWLEDGMENTS

We thank Scott Maclaren (UIUC MRL/CMM) for technical assistance. This work was supported by NSF Grants No. 1069076 and No. 1129826 (S. Z., T. L.), NSF-CMMI Grant No. 1130364 and NSF-NEB Grant No. 486171 (J. H. H., S. T. G., W. J. W., N. M.), and was carried out in part in the Frederick Seitz Materials Research Laboratory Central Facilities, University of Illinois.

[1] K. S. Kim, Y. Zhao, H. Jang, S. Y. Lee, J. M. Kim, K. S. Kim, J.-H. Ahn, P. Kim, J.-Y. Choi, and B. H. Hong, Large-scale pattern growth of graphene films for stretchable transparent electrodes, Nature (London) **457**, 706 (2009).

[2] S. Bae, H. Kim, Y. Lee, X. Xu, J.-S. Park, Y. Zheng, J. Balakrishnan, T. Lei, H. R. Kim, Y. I. Song, Y.-J. Kim, K. S. Kim, B. Ozyilmaz, J.-H. Ahn, B. H. Hong, and S. Iijima, Roll-to-roll production of 30-inch graphene films for transparent electrodes, Nat. Nanotechnol. **5**, 574 (2010).

[3] Y. Lee, S. Bae, H. Jang, S. Jang, S.-E. Zhu, S. H. Sim, Y. I. Song, B. H. Hong, and J.-H. Ahn, Wafer-scale synthesis and transfer of graphene films, Nano Lett. **10**, 490 (2010).

[4] R.-H. Kim, M.-H. Bae, D. G. Kim, H. Cheng, B. H. Kim, D.-H. Kim, M. Li, J. Wu, F. Du, H.-S. Kim, S. Kim, D. Estrada, S. W. Hong, Y. Huang, E. Pop, and J. A. Rogers, Stretchable, transparent graphene interconnects for arrays of microscale inorganic light emitting diodes on rubber substrates, Nano Lett. **11**, 3881 (2011).

[5] M. F. El-Kady, V. Strong, S. Dubin, and R. B. Kaner, Laser scribing of high-performance and flexible graphene-based electrochemical capacitors, Science **335**, 1326 (2012).

[6] S.-K. Lee, B. J. Kim, H. Jang, S. C. Yoon, C. Lee, B. H. Hong, J. A. Rogers, J. H. Cho, and J.-H. Ahn, Stretchable graphene transistors with printed dielectrics and gate electrodes, Nano Lett. **11**, 4642 (2011).

[7] C. Lee, X. Wei, J. W. Kysar, and J. Hone, Measurement of the elastic properties and intrinsic strength of monolayer graphene, Science **321**, 385 (2008).

[8] K. Kim, V. I. Artyukhov, W. Regan, Y. Liu, M. F. Crommie, B. I. Yakobson, and A. Zettl, Ripping graphene: Preferred directions, Nano Lett. **12**, 293 (2012).

[9] D. Sen, K. S. Novoselov, P. M. Reis, and M. J. Buehler, Tearing graphene sheets from adhesive substrates produces tapered nanoribbons, Small **6**, 1108 (2010).

[10] D. R. Cairns, R. P. Witte, D. K. Sparacin, S. M. Sachsman, D. C. Paine, G. P. Crawford, and R. R. Newton, Strain-dependent electrical resistance of tin-doped indium

oxide on polymer substrates, Appl. Phys. Lett. **76**, 1425 (2000).

[11] E. Fortunato, P. Nunes, A. Marques, D. Costa, H. Águas, I. Ferreira, M. E. V. Costa, M. H. Godinho, P. L. Almeida, J. P. Borges, and R. Martins, Influence of the strain on the electrical resistance of zinc oxide doped thin film deposited on polymer substrates, Adv. Eng. Mater. **4**, 610 (2002).

[12] X. Li, W. Cai, J. An, S. Kim, J. Nah, D. Yang, R. Piner, A. Velamakanni, I. Jung, E. Tutuc, S. K. Banerjee, L. Colombo, and R. S. Ruoff, Large-area synthesis of high-quality and uniform graphene films on copper foils, Science **324**, 1312 (2009).

[13] A. C. Ferrari, J. C. Meyer, V. Scardaci, C. Casiraghi, M. Lazzeri, F. Mauri, S. Piscanec, D. Jiang, K. S. Novoselov, S. Roth, and A. K. Geim, Raman Spectrum of Graphene and Graphene Layers, Phys. Rev. Lett. **97**, 187401 (2006).

[14] S. Scharfenberg, D. Z. Rocklin, C. Chialvo, R. L. Weaver, P. M. Goldbart, and N. Mason, Probing the mechanical properties of graphene using a corrugated elastic substrate, Appl. Phys. Lett. **98**, 091908 (2011).

[15] G.-H. Lee, R. C. Cooper, S. J. An, S. Lee, A. van der Zande, N. Petrone, A. G. Hammerberg, C. Lee, B. Crawford, W. Oliver, J. W. Kysar, and J. Hone, High-strength chemical-vapor-deposited graphene and grain boundaries, Science **340**, 1073 (2013).

[16] S. Zhu, Y. Huang, and T. Li, Extremely compliant and highly stretchable patterned graphene, Appl. Phys. Lett. **104**, 173103 (2014).

[17] S. Zhu and T. Li, Wrinkling instability of graphene on substrate-supported nanoparticles, J. Appl. Mech. **81**, 061008 (2014).

[18] J. Zang, S. Ryu, N. Pugno, Q. Wang, Q. Tu, M. J. Buehler, and X. Zhao, Multifunctionality and control of the crumpling and unfolding of large-area graphene, Nat. Mater. **12**, 321 (2013).

[19] Y. Wang, R. Yang, Z. Shi, L. Zhang, D. Shi, E. Wang, and G. Zhang, Super-elastic graphene ripples for flexible strain sensors, ACS Nano **5**, 3645 (2011).